

## A Differential DPSM Based Modeling Applied to Eddy Current Imaging Problems

Thierry Bore<sup>1, \*</sup>, Pierre-Yves Joubert<sup>2</sup>, and Dominique Placko<sup>1</sup>

**Abstract**—This paper deals with an innovative implementation of a semi-analytical modeling method, called the Distributed Points Source Method (DPSM), in the case of an eddy current problem. The DPSM has already shown great potentialities for the versatile and computationally efficient modeling of complex electrostatic, electromagnetic or ultrasonic problems. In this paper, we report a new implementation of the DPSM, called differential DPSM, which shows interesting prospects for the modeling of complex eddy current problems such as met in the non-destructive imaging of metallic parts. In this paper, the used eddy current imaging device is firstly presented. It is composed of an eddy current (EC) inducer and a magneto optical set-up used to translate the magnetic field distribution appearing at the surface of the imaged part, into a recordable optical image. In this study, the device is implemented for the time-harmonics (900 Hz) imaging of a two-layer aluminum based assembly, featuring surface-breaking and buried defects. Then, the basics of the time-harmonics DPSM modeling are recalled, and the differential approach is presented. It is implemented for the modeling of the interactions of the eddy current imaging device with the considered flawed assembly in the same operating conditions as the experimental implementation. The comparison between experimental and computed data obtained for millimetric surface and buried defects is presented in the form of complex magnetic cartographies and Lissajous plots. The obtained results show good agreement and open the way to the modeling of complex EC problems. Furthermore, the low computational complexity of the differential DPSM modeling makes it promising for solving EC inverse problems.

### 1. INTRODUCTION

Among the existing non-destructive testing (NDT) techniques, the eddy current (EC) method is widely used for the testing of electrically conductive media and has been rather popular for more than five decades for applications in nuclear or aeronautic industries. Indeed, the EC NDT is a reliable, non-contact, non-polluting, low cost and an easy to use technique, which is rather sensitive to defects such as cracks, inclusions or corrosion appearing in metallic structures [1]. The EC NDT technique is based on the Faraday's induction law: eddy currents are induced in an electrically conductive by means of a time-varying exciting magnetic field. In turn, the interactions of the induced EC with the media provoke a modification of the magnetic field distribution. The measurement of the resultant field at the surface of the tested structure may therefore provide relevant information about the inner features of the investigated media, such as geometry or electromagnetic changes possibly due to defects.

In order to turn the EC technique into an actual imaging technique, i.e., a technique able to evaluate the inner features of the tested media in a given inspection volume, it is necessary to i) elaborate an EC device able to provide relevant information relative to a sufficiently large inspection volume, ii) elaborate a model that can accurately foresee the three dimensional (3D) interactions between the EC device and the investigated part, and iii) solve the inverse problem that consists in estimating the features of the

---

*Received 24 March 2014, Accepted 28 May 2014, Scheduled 20 August 2014*

\* Corresponding author: Thierry Bore (bore.thierry@gmail.com).

<sup>1</sup> SATIE, ENS Cachan, CNRS, 61, avenue du président Wilson, 94 235 Cachan Cedex, France. <sup>2</sup> IEF, CNRS, Université Paris Sud, Bat. 220, 91405 Orsay Cedex, France.

part, in the considered volume, starting from the experimental data and using the interaction model [2]. As opposed to some other techniques such as X-ray, Gamma-Ray or ultrasonic imaging, the EC imaging technique is actually quite difficult to carry out in a quantitative manner. Indeed, because of the diffusive (and possibly diffractive) nature of the magnetic field propagation within the investigated media, EC devices lack sensitivity towards deep defects (skin effect) as well as spatial resolution when defects of small dimensions (cracks) are at stake [1, 3]. Furthermore, the measured magnetic field distribution does not directly match with the actual shape of the defects. So it is never immediate to characterize defect from the obtained EC data. As a consequence and since only EC data obtained at the surface of the inspected media are available, the associated inverse problem is actually “ill-posed” [2, 4], i.e., the solution of the problem may not be unique or even not exist.

So to elaborate a quantitative EC imaging technique in spite of these strong limitations, it is firstly necessary to dispose a 3D modeling of the EC interactions, which is both accurate and computationally efficient, so that the solving of the inverse problem can be made possible [2, 5].

The interactions of the EC device and the part are described by the Maxwell equations, the solving of which requires to determine the solution of a set of differential equations associated to limit conditions [5]. The exact solution leads to an analytical modeling, which will constitute the ideal modeling with regard to the inverse problem. However, the analytical solution is generally only reachable in simplified geometries [7–9] possibly associated with strong simplifying assumptions [3, 10, 11], so that it operates in a reduced validity domain.

In order to deal with more general cases, approximated numerical solutions such as the finite element (FE) method or the volume integral (VI) method may be preferred [5]. The FE method basically consists in the discretizing of the workspace into elemental sub-domains at the nodes of which the magnetic vector potential  $\vec{A}$  and the electric potential  $V$  are numerically estimated by means of a functional minimization process. Other electromagnetic variables may then be estimated by interpolation at any point of the workspace. This method may be seen as a universal modeling one since it allows any 3D EC problem to be dealt with. This method was applied in previous studies. In the first step, the FE method was applied to design the complete inducers. Different configurations of the inducting system were tested to obtain a more efficient configuration [12]. The FE method was then benchmarked by comparison with experimental data [13].

However, the computational cost may be too heavy to consider this method for inverse problem purposes. On the other hand, the VI method is based on an integral equation formulation and the use of Green functions which are the solutions of propagating equations of elementary current sources, including limit conditions relative to the geometric interfaces present in the workspace [14]. The VI method generally requires to only discretize the defective area within the media. The method is therefore computationally efficient and more likely to be successfully used in inverse problems approaches [15–18]. However, the model is generally only available for standard EC problem configurations and should be specifically derived for new or complex configurations [19, 20].

In our study, we consider an original modeling approach based on the distributed point source method (DPSM) [21]. The DPSM is a so-called mesh-free semi-analytical modeling method. Its basic principle is based on the modeling of the active sources present in the modeled workspace, by means of a set of elemental active sources and a set of equivalent source densities (ESD). The ESD are distributed at both sides of the boundaries separating the different media constituting the workspace and are determined considering the radiation of the actual active sources and the boundary conditions. The distributed sources (active sources as well as ESD) may be defined as elemental point sources, which radiate as Green’s functions in the considered media. The variables of interest at any point of the workspace may then be determined as the sum of the contribution of all radiating sources. The main advantages of the DPSM are that it is a “mesh-free” method (only the source network have to be actually meshed) and that workspaces including objects of any geometry may be modeled using such ESD, with no theoretical limitations on the shape and on the number of objects [22], as long as the considered media are isotropic and homogeneous. As a result, the DPSM constitutes a computationally efficient 3D modeling tool, which features great versatility, as already demonstrated in electrostatic problems [23, 24], in ultrasonic problems [25, 26], as well as electromagnetic problems [27] or coupled techniques (ultrasonics and electromagnetics [28]) with good prospects for the solving of inverse problems in EC applications [29, 30].

In this paper, the DPSM model is used in a so-called differential way to efficiently model an EC imaging device interacting with aluminum-alloy based metallic plates featuring machined calibrated notches. First, the used experimental set-up will be described in Section 2. In Section 3, the basic principle of the DPSM method derived for EC problems will be presented, and the differential implementation will be introduced. Section 4 will focus on the comparison between the obtained EC data and the modeling results, for various defect and operating configurations. Section 5 is on conclusions.

## 2. EDDY CURRENT IMAGING DEVICE AND EXPERIMENTAL SETUP

In this study, an eddy current imager (ECI) is considered. The ECI was firstly introduced in [31] and specifically designed for the quantitative imaging of large plane structures such as aeronautical riveted lap-joints [32, 33] or large diameter tank walls. As opposed to sensor arrays which are generally constituted of a network of transmit and receive elements mapping the inspection area [34, 35], the ECI basically consists in the combination of a large inducer, used to induce an uniformly oriented EC flow within the measurement area, and a magneto-optical (MO) set-up operated in polarized light. This set-up is used to translate, by Faraday effect, the magnetic field distribution appearing at the surface of the inspected area into an optical image that can be displayed and recorded (Figure 1).

The combination of the EC method with MO set-ups has been proven relevant for rapid imaging purposes in various NDT applications [35–37]. Indeed, these devices provide real time images of detected flaws in the inspected media. However, they only provide two-level quantized images, which, combined to a poor sensitivity to buried defects [36], are not suitable for quantitative defect imaging. The ECI implemented in this study uses a high sensitivity reversed U-shaped magnetic core inducer, fed with a current controlled power amplifier operating in time harmonics in the 100 Hz–50 kHz bandwidth. Due to its specific configuration [31], the inducer generates EC of uniform orientation within the measurement area located between the ends of the magnetic circuit of the inducer (Figure 1). In the presence of a defect, the modifications of the EC flow induce the apparition of a new magnetic field distribution, the normal component of which, appearing at the ends of the defect (Figure 2), is chosen to be imaged for efficient defect detection. To do so, a linear MO imaging film [38] is placed in the measurement area and included into a polarizer/analyzer optical set-up, so as to linearly translate the normal component of the complex magnetic field distribution, into grey level amplitude and phase images, thanks to a stroboscopic scheme [31]. The magnetic field images are computed thanks to a digital lock-in amplification scheme, and produced in the form of in-phase and in-quadrature images, determined by reference to the exciting

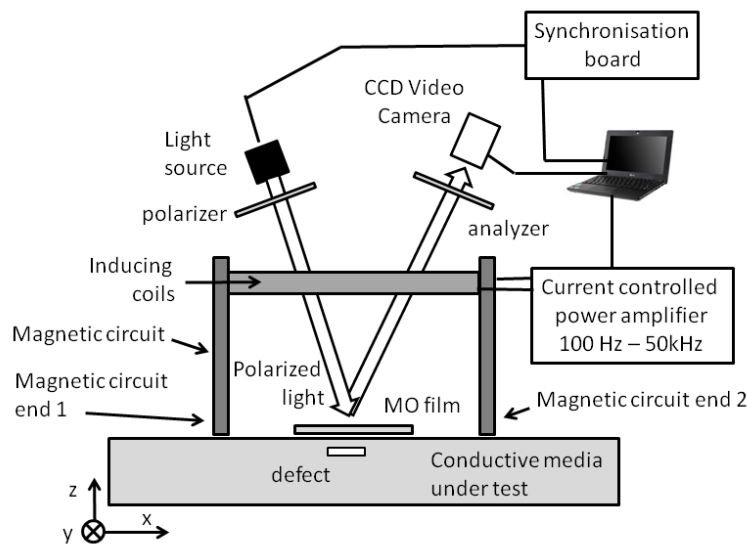


**Figure 1.** Schematic scheme of the eddy current imaging device (ECI) used in this study.

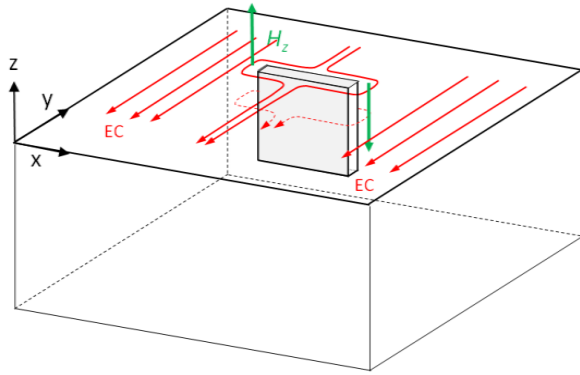


**Figure 2.** Interactions between ECs and a rectangular notch in a massive metallic part. ECs are uniformly oriented in absence of defects in the flawless area of the investigated volume.

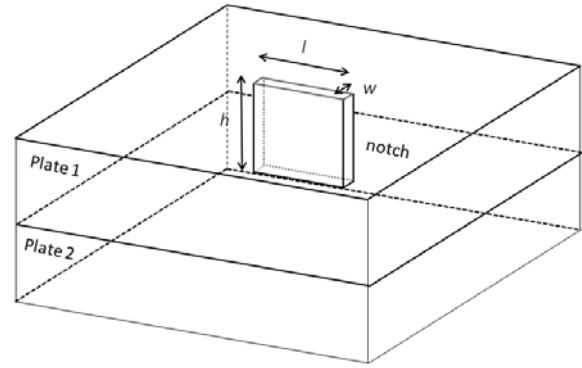


**Figure 3.** Mockup featuring a surface breaking calibrated notch.

current feeding the inducer, which is taken as phase-shift reference. As a result, the implemented ECI allows magnetic field distributions to be imaged in a 65 mm diameter measurement area, with a 72 dB measurement range and a  $100\ \mu\text{m} \times 100\ \mu\text{m}$  spatial resolution. Previous works also show that the ECI allows millimetric notches buried down to 7 mm in aluminum riveted lap joints to be detected [32].

In this paper, the ECI is implemented for the inspection of a two plate assembly mockups, featuring calibrated notches, as depicted in Figure 3. The used plates are 2 mm thick AL2024 T3 aluminum based alloy plates, featuring an electrical conductivity of 17 MS/m and a magnetic relative permeability of 1. Calibrated notches have been machined within the mockup. The dimensions of the considered notches are  $h = 2\ \text{mm}$ ,  $l = 8\ \text{mm}$  and  $w = 0.5\ \text{mm}$  (Figure 3). Two mockup configurations are considered here. The first one features a surface breaking notch (notch in plate 1, as depicted in Figure 3), and the second one features a 2 mm deep buried notch (notch in plate 2). In both configurations, the ECI is implemented with an EC frequency of 900 Hz, featuring a skin depth of 4 mm so as to investigate the whole thickness of the assembly. Also, the ECI is implemented in such a way that the induced EC flows perpendicularly to the notches. Examples of experimental EC images provided by the ECI for the investigation of the surface breaking defect are presented in Figure 6.

### 3. DPSM MODELING OF EC PROBLEMS

#### 3.1. DPSM Formalism in Electromagnetism

DPSM is a general purpose modeling method for the modeling of electrostatic, electromagnetic as well as ultrasonic problems. As previously pointed out, the method basically consists in the discretizing of the active sources of the workspace into a set of radiating point sources, and by dealing with material interfaces by using ESD, which are distributed at each side of the considered interfaces. ESD also radiates as point sources. The strength of ESD is initially unknown but is computed considering the electromagnetic boundary conditions at the interface between the considered materials. All physical values are then derived in the whole workspace from the summed contributions of all these radiating sources.

In the case of EC problems, both active sources and ESD are elemental current vectors. Each of these singularities radiates an electromagnetic field which can be computed by means of Green's functions, the total contribution being then derived without any heavy theoretical approximations since only Riemann summations are actually required. As a result, this modeling technique is very versatile and is able to work accurately in a wide range of frequencies, and for a wide range of physical properties of the materials (including geometry, electrical conductivity and permittivity, and magnetic permeability). Following the first step of global equating through a general matrix formulation, the problem is solved thanks to matrix inversion, which provides the values of all elemental sources. Therefore, it becomes

rather easy to compute fields and potentials in the whole volume of interest. The mathematical formulation of the problem is based on the calculation of the magnetic vector potential  $\vec{A}$  and its first derivatives (Equation (1)), and includes an important step for matching the boundary conditions at all interfaces between the different medias present in the workspace. In the second step, the global problem is solved, and then electric and magnetic fields may be computed in the whole workspace.

This part explains the DPSM formulation in EM where elemental sources are small current vectors. For these particular sources, the electromagnetic field radiated can be computed with the Green functions, introduced without any heavy theoretical approximations. So this modeling will be able to work accurately in a wide range of frequencies and for a wide range of physical properties of the materials (conductivity, electrical permittivity, and magnetic permeability). When the problem is solved, all the elemental values of the sources are well known, giving the ability to compute fields and potentials in all the media of the problem. The mathematical formulation used to solve the equations is based on the calculation of the magnetic vector potential  $\vec{A}_M$  and its first derivatives, and includes an important step concerning the matching of boundary conditions at the interfaces between different media. In the second step, the global problem is solved, and then electric and magnetic fields may be computed in the entire problem.

$$\begin{cases} \vec{A}_1 = \vec{A}_2 \\ \frac{1}{\mu_1} \cdot \frac{\partial \vec{A}_1}{\partial \vec{n}} = \frac{1}{\mu_2} \cdot \frac{\partial \vec{A}_2}{\partial \vec{n}} \end{cases} \quad (1)$$

From the Maxwell's equations, we can see that the electromagnetic field can be obtained by solving inhomogeneous wave equations.

$$\nabla^2 \vec{A} + k^2 \vec{A} = -\mu \cdot \vec{J} \quad (2)$$

where  $\vec{A}$  stands for the magnetic vector potential,  $\vec{J}$  the current density and

$$k^2 = \omega^2 \mu \varepsilon - j\omega \sigma \mu \quad (3)$$

with  $\varepsilon = \varepsilon_0 \cdot \varepsilon_r$  (with  $\varepsilon_0 = 1/36\pi \cdot 10^{-9}$ ) and  $\mu = \mu_0 \cdot \mu_r$  (with  $\mu_0 = 4\pi \cdot 10^{-7}$ ).

Green's theory allows an integral formulation of the problem, although the DPSM method uses a discrete formulation. We will see that after some assumptions, these equations fit nicely in the DPSM formulation when all source contributions are added at the observation point. Let  $G(\vec{r}, \vec{r}')$  be the response computed at position  $r$  due to a source located at  $r'$  (Dirac spatial pulse excitation) for an Helmholtz equation, which can be written as:

$$\nabla^2 G(\vec{r}, \vec{r}') + k^2 G(\vec{r}, \vec{r}') = \delta(\vec{r} - \vec{r}') \quad (4)$$

The solution of Equation (3) in a free homogeneous space is known as the Green's function and given in spherical coordinates by:

$$G(R) = -\frac{e^{-jkR}}{4\pi R} \quad (5)$$

Now, the particular solution to excitation  $\vec{J}(\vec{r}')$  can be obtained by applying the convolution integral. This solution can be written as:

$$\vec{A}(\vec{r}) = \mu \cdot \iiint_V \vec{J}(\vec{r}') \cdot G(R) \cdot dv' = \frac{\mu}{4\pi} \cdot \iiint_V \vec{J}(\vec{r}') \cdot \frac{e^{-jkR}}{R} \cdot dv' \quad (6)$$

Magnetic and electric fields  $\vec{B}$  and  $\vec{E}$  can be obtained from:

$$\vec{B}(\vec{r}) = \text{rot } \vec{A}(\vec{r}) \quad \text{and} \quad \vec{E} = -\frac{\partial \vec{A}}{\partial t} \quad (7)$$

According to the DPSM formulation, the term  $\vec{J}$  represents a finite sum of  $N_s$  number of point sources:

$$\vec{J}(\vec{r}') = \sum_{i=1}^{N_s} \vec{J}_i \cdot \delta(\vec{r}' - \vec{r}_i) \quad (8)$$

Which leads to:

$$\vec{A}(\vec{r}) = \mu \cdot \sum_{i=1}^{N_s} \vec{J}_i \cdot \iiint_v G(\vec{r} - \vec{r}') \cdot \delta(\vec{r}' - \vec{r}_i) dv = \mu \cdot \sum_{i=1}^{N_s} \vec{J}_i \cdot G(\vec{r} - \vec{r}_i) \quad (9)$$

Comparing Equations (6) and (9) we can conclude that  $\vec{J}_i$  is equivalent to the current density  $\vec{J}(\vec{r}')$  which has been integrated on a small elemental volume  $dv$ , and then it represents an elemental source vector (triplet source) with three  $x$ ,  $y$ , and  $z$  components, whose units are current multiplied by a length, or A.m.

In Cartesian coordinates, the vector potential calculated at a point of coordinate  $\vec{r}$  can be written as:

$$\vec{A}(\vec{r}) = \begin{cases} \frac{\mu}{4\pi} \cdot \sum_i Jx_i \cdot \frac{e^{-jkR_i}}{R_i} \\ \frac{\mu}{4\pi} \cdot \sum_i Jy_i \cdot \frac{e^{-jkR_i}}{R_i} \\ \frac{\mu}{4\pi} \cdot \sum_i Jz_i \cdot \frac{e^{-jkR_i}}{R_i} \end{cases} = \begin{cases} Ax(\vec{r}) \\ Ay(\vec{r}) \\ Az(\vec{r}) \end{cases} \quad (10)$$

$$\text{with } \vec{R}_i = \vec{r} - \vec{r}_i = \begin{cases} x - Cx_i \\ y - Cy_i \\ z - Cz_i \end{cases} \quad \text{and } \|\vec{R}_i\| = R_i = \sqrt{(x - Cx_i)^2 + (y - Cy_i)^2 + (z - Cz_i)^2}.$$

### 3.2. Matrix Formulation

The DPSM formulation adds the contributions of all point sources computed at a given array of observation points  $P$ . For example, let us assume that we have  $N_p$  observation points. So, for every value of  $r_j$ , the magnetic vector potential  $\vec{A}(\vec{r}_j)$  is composed of three vectors:  $\vec{A}x$ ,  $\vec{A}y$  and  $\vec{A}z$ . For example,  $\vec{A}x$  is given by:

$$\vec{A}x = \frac{\mu}{4\pi} \begin{bmatrix} \frac{e^{-jkR_{11}}}{R_{11}} & \cdots & \cdots & \frac{e^{-jkR_{1N_s}}}{R_{1N_s}} \\ \vdots & & & \vdots \\ \vdots & & & \vdots \\ \frac{e^{-jkR_{N_p1}}}{R_{N_p1}} & \cdots & \cdots & \frac{e^{-jkR_{N_pN_s}}}{R_{N_pN_s}} \end{bmatrix} \cdot \vec{J}x \Leftrightarrow \vec{A}x = [Wxx] \cdot \vec{J}x \quad (11)$$

This example sets in evidence one of the important step in DPSM: we can easily define a coupling matrix for computing on a set of  $N_p$  observation points the effect of an array of  $N_s$  sources. This matrix is also defined in a particular case, in which the array of observation points matches with the array of test points. Then, we define the  $W_{aj}$  matrix for computing the vector potential on array of test points "a" due to the array of sources "j", and the  $Y_{aj}$  matrix for first derivative of the vector potential on array of test points "a" due to the array of sources "j".

### 3.3. Implementation of the DPSM Modeling

In this study, we propose a so-called differential implementation of the DPSM, so as to focus the modeling on the magnetic field appearing at the surface of the investigated part and resulting from a defect present within the part, independent from the used inducer. This approach enables the computation effort required to model the interactions between the ECI and the defects in the part to be significantly reduced, as presented in this section.

In the first step, an equivalent inducer of reduced dimensions is considered for the modeling. This equivalent inducer is composed of two rectangular excitation air coils (without magnetic circuit),

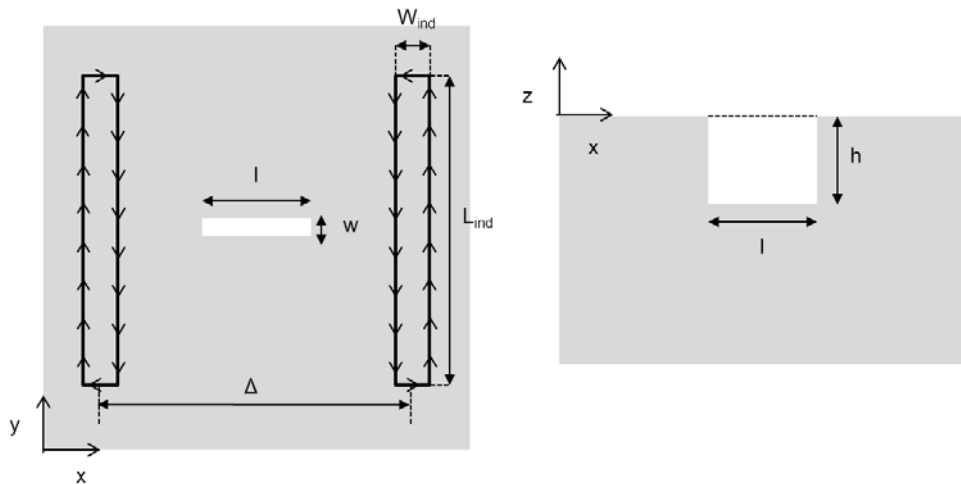


**Figure 4.** Simplified configuration: driving currents and surface crack.

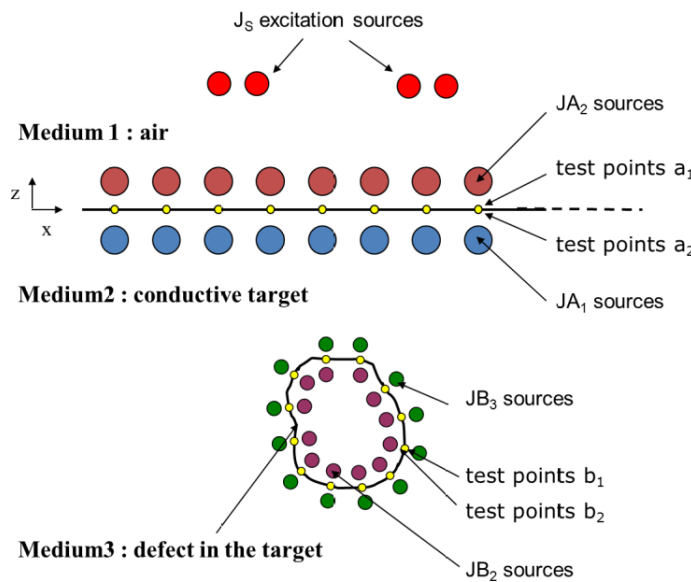


**Figure 5.** Illustration of the DPSM configuration of an eddy current problem with a crack (in the plane  $XOZ$ ).

featuring a  $L_{ind} = 32$  mm length and a  $W_{ind} = 3$  mm width. These two coils are placed at a distance of  $\Delta = 40$  mm from one another along the  $X$  axis, as depicted in Figure 4. In the absence of defect, this inducer generates an eddy current flow which is uniform in intensity and in direction in a large inspection area, as for the actual inducer. This was checked in a previous study [27]. The medium under inspection is a semi-infinite medium along the  $Z$  axis. The size of the interface is 60 by 60 mm. This dimension has to be large enough to avoid edge effect.

The DPSM configuration used for modeling the general problem (i.e., considering a part with a defect of any shape) is sketched on Figure 5. The inducing coils are meshed with a set of sources called  $J_S$  featuring  $N_c$  sources. The interface between air (upper medium) and conductive target (lower medium) is meshed with the set of observation points  $a_1$  and  $a_2$  on which the interface continuity conditions are applied. These particular observations points placed at the interface are called test points. Please note that the interfaces are meshed with a number of test points satisfied at much more than 3 points

over the skin depth (or the wavelength) [22]. They are associated with two sets of sources denoted  $JA_1$  and  $JA_2$ , which gather the sources radiating into medium 1 and the sources radiating into medium 2, respectively. The numbers of sources in  $JA_1$  and  $JA_2$  are chosen to be equal: there are  $N_a$  sources at each side of the interface. Finally, the same meshing procedure is applied to the defect present in the part, i.e., it is meshed thanks to  $N_b$  test points  $b_2$  and  $b_3$ , constituting the test sets  $JB_2$  and  $JB_3$ , as described in Figure 5. More details on this formulation can be found in [27].

By using the elemental coupling matrixes between the different elements of this problem, we can regroup all the boundary equations in a global matrix form. The unknown parameters are the values of the point sources; they are obtained by solving the system of linear equations given in Equation (12) linking the vector of all the DPSM sources  $J$  to a vector of boundary conditions  $C$ .

$$C = M \cdot J \quad (12)$$

With:

$$J = \begin{pmatrix} J_S \\ JA_1 \\ JA_2 \\ JB_2 \\ JB_3 \end{pmatrix} \quad \text{and} \quad C = \begin{pmatrix} J_S \\ 0 \\ 0 \\ 0 \\ 0 \end{pmatrix} \quad (13)$$

$$M = \begin{pmatrix} I & 0 & 0 & 0 & 0 \\ W_{a_1 J_S} & W_{a_1 J_{A_1}} & -W_{a_2 J_{A_2}} & -W_{a_2 J_{B_2}} & 0 \\ \frac{1}{\mu_1} Y_{a_1 J_S} & \frac{1}{\mu_1} Y_{a_1 J_{A_1}} & -\frac{1}{\mu_2} Y_{a_2 J_{A_2}} & -\frac{1}{\mu_2} Y_{a_2 J_{B_2}} & 0 \\ 0 & 0 & W_{b_2 J_{A_2}} & W_{b_2 J_{B_2}} & -W_{b_3 J_{B_3}} \\ 0 & 0 & \frac{1}{\mu_2} Y_{b_2 J_{A_2}} & \frac{1}{\mu_2} Y_{b_2 J_{B_2}} & -\frac{1}{\mu_3} Y_{b_3 J_{B_3}} \end{pmatrix} \quad (14)$$

with  $I$  the  $3N_c \times 3N_c$  identity matrix. Note that the global matrix  $M$  is always square, which has a size of  $3(N_c + 2N_a + 2N_b) \times 3(N_c + 2N_a + 2N_b)$ . By inverting the matrix, we can find the strength of all DPSM sources and be allowed now to calculate the field values everywhere in the space containing our problem.

### 3.4. Differential Formulation

The main advantage of DPSM modeling is that the derivation leads to analytical results. So, it is easy to equate the problem for two different conditions (for example with two different properties of the medium 3 into the crack), and to make the difference to see the effect of this variation. Keeping our example, the purpose is to see the effect of the crack on the signal measured at the surface of the material under test. It becomes easy to perform two different modelings, the first one with a crack filled with a medium 3 identical to medium 2 and the second one performed with a medium 3 different from medium 2. This is called ‘differential DPSM’ in the following of this paper. Let us now derive the corresponding set of equations.

The differential modeling requires the resolution of two DPSM problems. The first, called reference state, corresponds to the case where the physical properties of the crack are equal to the properties of the target. Here, we do not consider dielectric or magnetic properties of the medium (e.g.,  $\varepsilon_r = \mu_r = 1$ ). Then, the reference state is characterized by  $\sigma_3 = \sigma_2$ . The global matrix form of this state is defined by the following equation:

$$C = M^{\sigma_3 = \sigma_2} \cdot J^{\sigma_3 = \sigma_2} \quad (15)$$

In the same way, any state characterized by  $\sigma_3 \neq \sigma_2$  has the following global matrix form:

$$C = M^{\sigma_3 \neq \sigma_2} \cdot J^{\sigma_3 \neq \sigma_2} \quad (16)$$

Moreover, we can link both states with the equation:

$$\begin{cases} J^{\sigma_3 \neq \sigma_2} = J^{\sigma_3 = \sigma_2} + \Delta J \\ M^{\sigma_3 \neq \sigma_2} = M^{\sigma_3 = \sigma_2} + \Delta M \end{cases} \quad (17)$$

Then, we can rewrite Equation (16):

$$C = M^{\sigma_3 \neq \sigma_2} \cdot (J^{\sigma_3 = \sigma_2} + \Delta J) \tag{18}$$

By subtracting Equation (18) and Equation (15), we can obtain:

$$0 = (M^{\sigma_3 \neq \sigma_2} - M^{\sigma_3 = \sigma_2}) \cdot J^{\sigma_3 = \sigma_2} + M^{\sigma_3 \neq \sigma_2} \cdot \Delta J \tag{19}$$

This yields:

$$\Delta M \cdot J^{\sigma_3 = \sigma_2} = -M^{\sigma_3 \neq \sigma_2} \cdot \Delta J \tag{20}$$

Equation (20) allows us to compute new  $\Delta J$  sources corresponding to a configuration where the sources due to the inducers have vanished. This way of modeling will be used in the next section to compute the magnetic field radiated at the upper surface of the material, only due to the crack effect as in the ECI.

#### 4. MODELING RESULTS VS ECI MEASUREMENTS

In this section, the EC images provided by the ECI implemented in the operating conditions described in Section 2 are compared to the magnetic field cartographies issued from the DPSM model, as described in Section 3, when applied to the same configuration.

Figures 6(a) and 6(b) respectively show the in-phase and in-quadrature EC images delivered by the ECI when used above the two-plate assembly featuring the surface breaking notch (see Figure 3). Figures 7(a) and 7(b) respectively show the in-phase and in-quadrature EC images computed by means of the DPSM for the same configuration. In both cases, the excitation frequency of 900 Hz was chosen as a frequency enabling the whole thickness of the part to be investigated (skin depth is 4 mm in the aluminum alloy at 900 Hz).

In order to compare experimental and computed data, note that a normalization of the amplitude has been necessary, since the EC images provided by the ECI are issued from a magneto-optical translation, as the DPSM directly provides EC images which are magnetic field values. After normalization, it can be noted that the agreement between computations and experimental images is quite satisfactory. The notch is roughly located between the two extremes peaks of the images.

The second comparison is provided in Figure 8, which exhibits the Lissajous plots (in-quadrature vs in-phase data) of the EC data obtained along a cut line joining the ends of the notch, in the case of experimental and computed data. Here again, one can note the good agreement between experimental and computed data after amplitude normalization. A third example is provided in Figure 9. Here, the assembly featuring the notch buried in plate 2 (i.e., under 2 mm of aluminum) is considered.

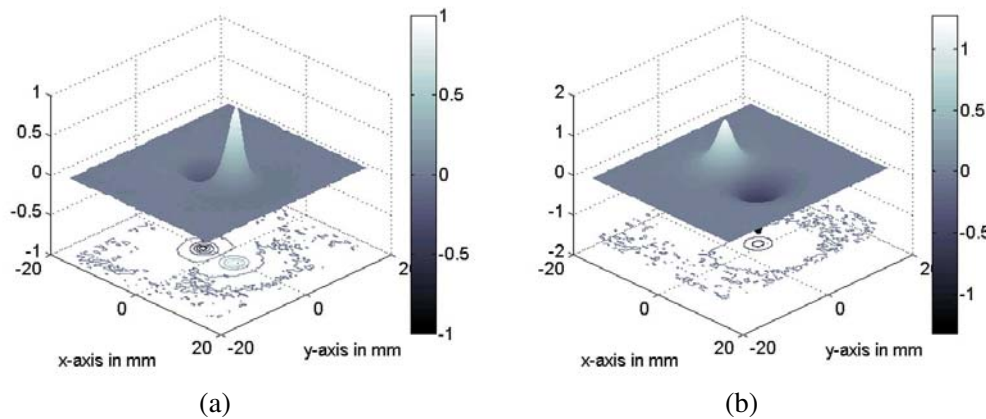


**Figure 6.** Experimental EC images obtained at 900 Hz for the surface breaking notch. (a) In-phase image, (b) in-quadrature image. Amplitudes are in arbitrary units.

The Lissajous plots obtained for this configuration also show a good agreement between experimental and computed data, after amplitude normalization, even if experimental data exhibits an altered signal to noise ratio, due to the depth of the notch.

Starting from these encouraging results, it was interesting to run our DPSM model for different kinds of configurations. Some of these results are presented here, particularly the effect of the depth of the defect on the EC data. Computations of the magnetic field were realized at 900 Hz for different values of the notch depth (noted  $\Delta z$  in the following) ranging in the depth set  $\{0, 5, 250, 500, 1000, \text{ and } 1500\}$  expressed in  $\mu\text{m}$ . The Lissajous plots obtained for various values of  $\Delta z$  are represented in Figure 10.

Then, the phase-shift obtained for the maximum value of the modulus of the magnetic field was determined and plotted versus  $\Delta z$  in Figure 11. The experimental data are also represented in this figure.

It can be noted that the phase linearly depends on the crack depth, and a linear regression gives a root mean square deviation equal to 0.007.

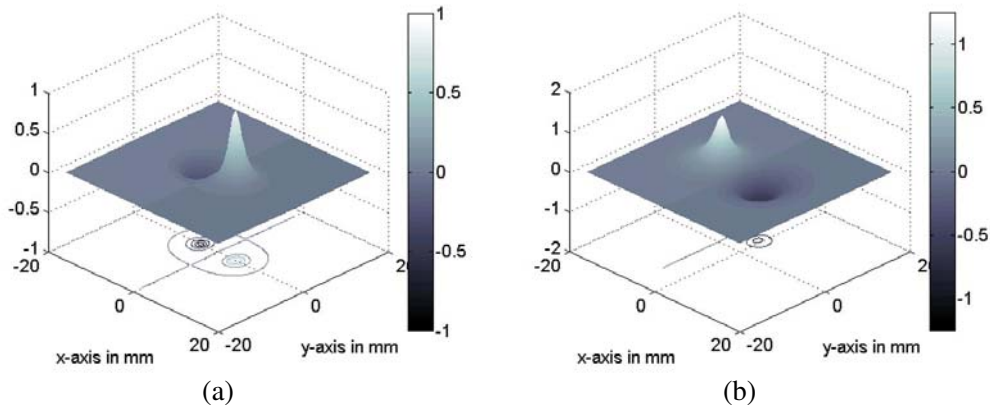


**Figure 7.** Computed EC images obtained at 900 Hz for the surface breaking notch. (a) In-phase image, (b) in-quadrature image. Amplitudes are in arbitrary units.

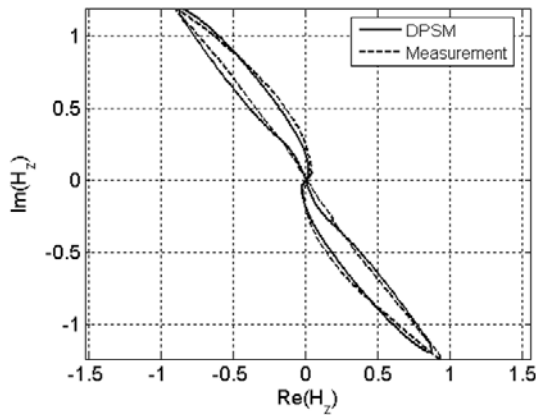


**Figure 8.** Comparison between experimental and computed Lissajous plots for EC data along a cut line joining the ends of the notch ( $X$  axis) obtained at 900 Hz for the surface defect.  $\text{Re}(H_z)$  and  $\text{Im}(H_z)$  designate the in-phase and in-quadrature parts of the magnetic field, respectively.

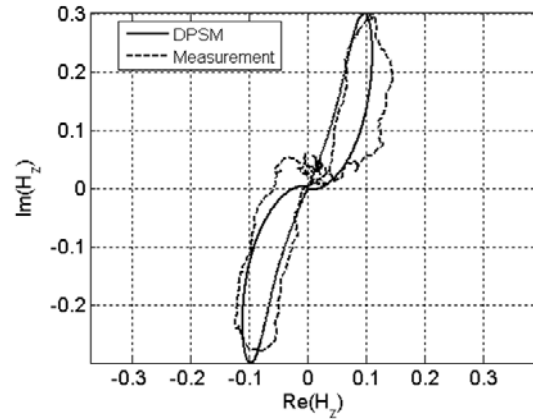


**Figure 9.** Comparison between experimental and computed Lissajous plots for EC data along a cut line joining the ends of the notch ( $X$  axis) obtained at 900 Hz for the 2 mm deep buried notch.  $\text{Re}(H_z)$  and  $\text{Im}(H_z)$  designate the in-phase and in-quadrature parts of the magnetic field, respectively.

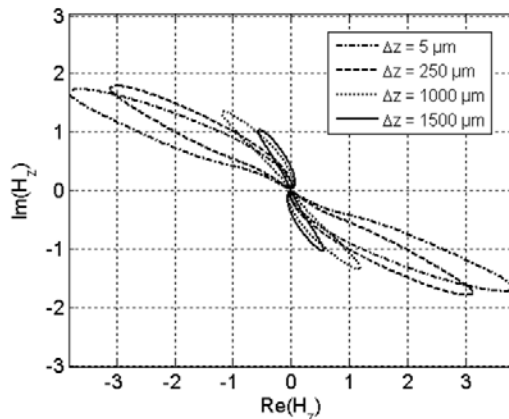


**Figure 10.** Computed Lissajous plots along a cut line parallel to the  $X$  axis obtained at 900 Hz for different depth of the buried defect.  $\text{Re}(H_z)$  and  $\text{Im}(H_z)$  designate the in-phase and in-quadrature parts of the magnetic field, respectively.

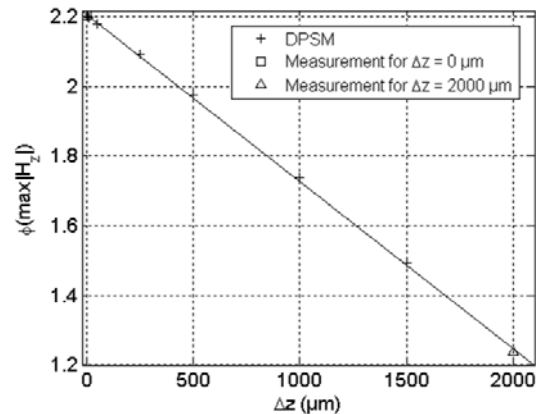


**Figure 11.** Comparison between experimental and computed Lissajous plots along a cut line parallel to the  $X$  axis obtained at 900 Hz for notches buried at  $\Delta z$ .

As it can be seen on these figures, the DPSM allows various crack depths to be considered, even for very small values of the remaining thickness between the top of the defect and the surface of the material. In the case of finite elements methods, changing the crack depth induces new meshing, with additional difficulty for very small thicknesses.

It is obvious that only selected results were presented here, and in fact, the DPSM modeling can provide a lot of interesting data reflecting our ECI sensor behavior. For example, it is possible to put in the defect a material with given electrical properties, such as adjustable conductivity, and to see the effect of this conductivity variation on the output signals. This is particularly interesting for studying the case of corrugated materials for example. It is also possible to run the model in parametric mode for sensor design optimizations. Applied to the ECI case, various configurations may be studied to optimize the ratio efficiency/size of the inducer, or to optimize the eddy current phase value in the area of interest.

## 5. CONCLUSIONS

In this paper, some original properties and theoretical extensions of the Distributed Point Source Method (DPSM) are presented. This method extension, called differential DPSM, has been discussed and applied to an Eddy current sensor modeling, leading to interesting comparisons between experimental and theoretical data. Then, this method opens the way to quantitative imaging, in which the differential DPSM will serve as a direct modeling in an inversion scheme [39]. Furthermore, this generic method is applicable to other techniques, such as ultrasonics or electrostatics. The basic principles of DPSM make this method able to solve coupled problems, such as electromagnetic acoustic transducers. In addition, this method may be used in a parametric mode, to study, in more details, the effects of multiple variations of the properties of the device under test, or to optimize a sensor design.

## REFERENCES

1. Udpa, S. and P. Moore, *Nondestructive Testing Handbook*, 3rd Edition, Vol. 5, Electromagnetic Testing, American Nondestructive Testing Society, 2004.
2. Cacciola, M., F. C. Morabito, D. Polimeni, and M. Versaci, "Fuzzy characterization of flawed metallic plates with eddy current tests," *Progress In Electromagnetics Research*, Vol. 72, 241–252, 2007.

3. Libby, H. L., *Introduction to Electromagnetic Nondestructive Test Methods*, Robert Krieger Publisher Company, New York, 1979.
4. Yusa, N., H. Huang, and K. Miya, "Numerical evaluation of the ill-posedness of eddy current problems to size real cracks," *NDT and E Int.*, Vol. 40, No. 3, 185–191, 2007.
5. Prémel, D. and A. Baussard, "Eddy current evaluation of 3D flaws in flat conductive materials using a Bayesian approach," *Inv. Problems*, 1873–1889, 2002.
6. Ida, N., *Numerical Modeling for Electromagnetic Non Destructive Evaluation*, Chapman & Hall, 1995.
7. Dodd, C. V. and W. E. Deeds, "Analytical solutions to eddy-current probe-coil problems," *J. Appl. Phys.*, Vol. 39, 2829, 1968.
8. Uzal, E., J. C. Moulder, S. Mitra, and J. H. Rose, "Impedance of coil over layered metals with continuously variable conductivity and permeability, theory and experiment, probe-coil problems," *J. Appl. Phys.*, Vol. 74, 2076, 1970.
9. Mukerji, S. K., M. George, M. B. Ramamurthy, and K. Asaduzzaman, "Eddy currents in laminated rectangular cores," *Progress In Electromagnetics Research*, Vol. 83, 435–445, 2008.
10. Burke, S. K., "Impedance of a horizontal coil above a conducting half space," *Journal of Physics D: Applied Physics*, Vol. 19, 1159–1173, 1986.
11. Le Bihan, Y., "Study on the transformer equivalent circuit of eddy current nondestructive evaluation," *NDT and E Int.*, Vol. 36, No. 5, 297–302, Jul. 1, 2003.
12. Le Diraison, Y., "Imagerie à courants de Foucault pour l'évaluation non-destructive de structures rivetées aéronautiques," Ph.D. Thesis, École normale supérieure de Cachan-ENS Cachan, 2008.
13. Le Diraison, Y., P.-Y. Joubert, and J. Pinassaud, "3D finite element modeling of an eddy current imager," *7th International Symposium on Electric And Magnetic Fields*, 99–100, Aussois, France, Jun. 19–22, 2006.
14. Bowler, J. R., "Eddy current calculations using half-space Green's functions," *J. Appl. Phys.*, Vol. 61, 833–839, 1987.
15. Dodd, C. V. and W. E. Deed, "Integral solutions to some eddy current problems," *International Journal of Non Destructive Testing*, Vol. 1, 29–90, 1969.
16. Albanese, R., G. Rubinacci, and F. Villone, "An integral computation model for crack simulation and detection via eddy currents," *J. Comput. Phys.*, Vol. 152, 736–735, 1999.
17. Rubinacci, G., A. Tamburrino, S. Ventre, F. Villone, L. Udpa, L. Xuan, and Z. Zeng, "Numerical simulation of magneto-optic eddy current imaging," *Electromagnetic Nondestructive Evaluation (VII)*, 180–188, G. Dobmann (eds.), IOS Press, 2006.
18. Premel, D. and P. Baussard, "Eddy current evaluation of 3D flaws in flat conductive materials using a Bayesian approach," *Inv. Problems*, 1873–1889, 2002.
19. Rubinacci, G., A. Tamburrino, S. Ventre, P.-Y. Joubert, and J. Pinassaud, "Numerical modeling of phase sensitive eddy current imaging system," *Studies in Applied Electromagnetics and Mechanics, Electromagnetic Non-destructive Evaluation (X)*, Vol. 28, 33–40, IOS Press, 2007.
20. Paillard, S., G. Pichenot, Y. Choua, Y. Le Bihan, M. Lambert, H. Voillaume, and N. Dominguez, "Modelling of flawed riveted structures for EC inspection in aeronautics," *Studies in Applied Electromagnetics and Mechanics, Electromagnetic Nondestructive Evaluation (XI)*, Vol. 31, 217–224, IOS Press, 2008.
21. Placko, D., T. Kundu, N. Liebaux, and A. Cruau, "Procédé universel de modélisation des interactions entre au moins une onde et au moins un objet, la surface de chaque objet définissant une interface entre au moins deux milieux," French patent No. FR2895544B1, Dec. 23, 2005; Patent Application Canada No. CA2634903A1, Dec. 20, 2006; Patent Application Japon No. JP2008-546450A1, Dec. 20, 2006; Patent Application USA No. US2010-0010781A1, Dec. 20, 2006.
22. Placko, D. and T. Kundu, *DPSM for Modeling Engineering Problems*, John Wiley & Sons, Inc., Hoboken, New Jersey, 2007.
23. Bore, T., D. Placko, F. Taillade, and M. Himbert, "Capacitive sensor for measuring the filled of post-tensioned ducts. Experimental set-up, modelling and signal processing," *IEEE Sensors*

- Journal*, Vol. 13, 457–465, 2013.
24. Bore, T., D. Placko, F. Taillade, and P. Sabouroux, “Electromagnetic characterization of grouting materials of bridge post tensioned ducts for NDT using capacitive probe,” *NDT and E Int.*, Vol. 60, 110–120, 2013.
  25. Placko, D. and T. Kundu, “Ultrasonic nondestructive evaluation: Engineering and biological material characterization,” 143–202, T. Kundu (Ed.), Pub. CRC Press, 2004.
  26. Kundu, T., D. Placko, S. Das, and T. Bore, “Modeling of ultrasonics fields by distributed point source method,” *Ultrasonic and Electromagnetic NDE for Structure and Material Characterization: Engineering and Biomedical Applications*, 109–166, CRC Press, 2012.
  27. Placko, D., T. Bore, and T. Kundu, “Distributed point source method for imaging in electrostatic and electromagnetic problems,” *Ultrasonic and Electromagnetic NDE for Structure and Material Characterization: Engineering and Biomedical Applications*, 249–295, CRC Press, 2012.
  28. Eskandazade, M., T. Kundu, N. Liebeaux, D. Placko, and F. Mobadersani, “Numerical simulation of electromagnetic acoustic transducers using distributed point source method,” *Ultrasonics*, Vol. 50, No. 6, 583–591, 2010.
  29. Joubert, P.-Y., E. Vourc’h, and D. Placko, “Qualitative reconstruction of defects in oriented field eddy current magneto-optical imaging,” *Proceedings of 14th International IGTE Symposium on Numerical Field Calculation in Electrical Engineering*, Graz, Austria, Sep. 19–22, 2010.
  30. Bausson, S., V. Thomas, P.-Y. Joubert, L. Blanc-Ferraud, J. Darbon, and G. Aubert, “Regularized inversion of a distributed point source model for the reconstruction of defects in eddy currents imaging,” *COMPEL*, Vol. 30, No. 6, 1777–1791, 2011.
  31. Joubert, P.-Y. and J. Pinassaud, “Linear magneto-optic imager for non-destructive evaluation,” *Sensors and Actuators A*, Vol. 129, 126–130, 2006.
  32. Le Diraison, Y., P.-Y. Joubert, and D. Placko, “Characterization of subsurface defects in aeronautical riveted lap-joints using multi-frequency eddy current imaging,” *NDT and E Int.*, Vol. 42, No. 2, 133–140, 2009.
  33. Mook, G., F. Michel, and J. Simonin, “Electromagnetic imaging using probe arrays,” *17th World Conference on Nondestructive Testing, WCNDT 2008*, Shanghai, China, Oct. 2008.
  34. Marchand, B., J. M. Decitre, and O. Casula, “Flexible and array eddy current probes, for fast inspection of complex parts,” *Review of Quantitative Nondestructive Evaluation*, Vol. 29, 313–320, D. O. Thompson, D. E. Chimenti (Eds.), American Institute of Physics, 2010.
  35. Novotny, P., P. Saddl, and P. Machac, “A magneto-optic imager for NDT applications,” *NDT and E Int.*, Vol. 37, No. 8, 645–649, 2004.
  36. Office of Aviation Research, “Development of an improved magneto optic/eddy current imager,” Final Report DOT/FAA/AR-97/37, 20591, Washington DC, 1998.
  37. Le, M., J. Lee, and T. Shoji, “A simulation of magneto-optical eddy current imaging,” *NDT and E Int.*, Vol. 44, 783–788, 2011.
  38. Grechishkin, R., S. Chigirinski, M. Gusev, O. Cugat, and N. Dempsey, *Magnetic Imaging Films, Magnetic Nanostructures in Modern Technology*, 195–224, Springer, Berlin, 2008.
  39. Placko, D., T. Bore, and A. Rivolet, “Imaging and detection of cracks in metallic structures with eddy current sensors,” *SPIE — Smart Structures/NDE Proceedings*, San Diego, California, 2013.